Polyhedron 242 (2023) 116492

Contents lists available at ScienceDirect

Polyhedron

journal homepage: www.elsevier.com/locate/poly

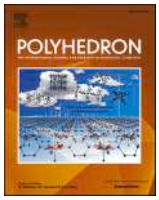

Improved photoluminescence properties of one-dimensional (1D) composite fibers of Ho@PVP and Yb@PVP prepared by electrospinning

Fatma Kuru [a], Mustafa Burak Coban [b,*], Ugur Erkarslan [a], Adem Donmez [a,c], Gorkem Oylumluoglu [a], Muhittin Aygun [d], Hulya Kara Subasat [a,e]

[a] Department of Physics, Faculty of Science, Molecular Nano-Materials Laboratory, Mugla Sıtkı Koçman University, Mugla, Turkey
[b] Science and Technology Research and Application Center, Balikesir University, Balikesir, Turkey
[c] Department of Electricity and Energy, Yatagan Vocational School, Mugla Sitki Kocman University, Mugla, Turkey
[d] Department of Physics, Faculty of Science and Art, Dokuz Eylul University, Izmir, Turkey
[e] Department of Energy, Graduate School of Natural and Applied Sciences, Mugla Sıtkı Kocman University, Mugla, Turkey

ARTICLE INFO

Keywords:
Electrospinning
Ho^{3+} and Yb^{3+} Luminescent fiber
Polyvinylpyrrolidone (PVP)
Rare earth compound
Crystal structure

ABSTRACT

Two new Holmium^{3+} and Ytterbium^{3+} compounds, {Ho(4cba)$_3$(phen)(H$_2$O)} (**1**) and {Yb(4cba)$_3$(phen)} (**2**) (4cba = 4-Cyanobenzoic acid, phen = 1,10-Phenanthroline) were synthesized. These compounds were then incorporated into a Polyvinylpyrrolidone (PVP) matrix at different concentrations (5 wt% to 25 wt%) using an electrospinning technique, resulting in the formation of 1D luminescent composite fibers, Ho@PVP and Yb@PVP. The products were analyzed using various characterization techniques to determine their structures and morphologies. A comprehensive study was conducted to investigate the thermal and photoluminescence properties of these composite nanofibers in comparison to their pure compounds. The findings revealed significant enhancements in the photostability and thermal stability of the composite nanofibers due to the solid environment provided by PVP for the compounds. Furthermore, it was observed that the composite nanofibers exhibited notably superior the thermal-stability and the photo-stability when compared to their pure compounds.

1. Introduction

Lanthanide compounds have recently gained significant attention for their fundamental investigations and applications in various fields such as luminescent probes, drug delivery, optoelectronics, optical communications, and sensors [1–7]. These compounds exhibit emission bands resulting from f-f transitions [8], which have an extremely narrow bandwidth and therefore produce highly pure colors in emitted light [9,10]. Considering the fundamental emissive characteristics, Ho^{3+} ions play a crucial role as activator ions due to their broad photoluminescence (PL) spectrum, spanning from the visible to the infrared (IR) range, and their strong yellow emission. The efficient yellow emission of Ho^{3+} ions finds applications in diverse fields such as solid-state lighting devices, field emission displays, and security printing, as well as biological and sensing applications. Meanwhile, Yb^{3+} ions, which exhibit near-infrared (NIR) luminescence at approximately 980 nm, are considered highly promising candidates with vast application prospects in the fields of bioanalytical research, telecommunications, and laser design systems [11].

In recent years, there has been growing interest in luminescent nanocomposites [12]. Various techniques, including self-assembly [13], solution casting [14], phase separation [15], melt blowing [16], and chemical methods [17], have been employed for the fabrication and synthesis of composite materials. Among these methods, electrospinning stands out as the simplest and most effective technique for producing continuous 1D hybrid composite fibers at the nanoscale [18]. By adjusting the electrospinning parameters, a wide range of structures can be achieved, including porous fibers, ribbon structures, wrinkled structures, beaded fibers, and others [19–22]. Electrospinning has been successfully used to obtain luminescent composite fibers with optical properties using various polymers such as polyvinyl alcohol (PVA), polyethylene oxide (PEO), polymethyl methacrylate (PMMA), and polyvinyl pyrrolidone (PVP) [23,24]. PVP, being a synthetic polymer, has garnered significant research interest due to its remarkable characteristics. It exhibits high complexation ability, excellent hydrophilicity, exceptional ultimate tensile strength, elasticity, corrosion resistance, and a strong affinity for water [25]. Additionally, PVP demonstrates low chemical toxicity and possesses reasonable solubility in both water and

* Corresponding author.
E-mail address: burakcoban@balikesir.edu.tr (M.B. Coban).

https://doi.org/10.1016/j.poly.2023.116492
Received 7 April 2023; Accepted 3 June 2023
Available online 7 June 2023

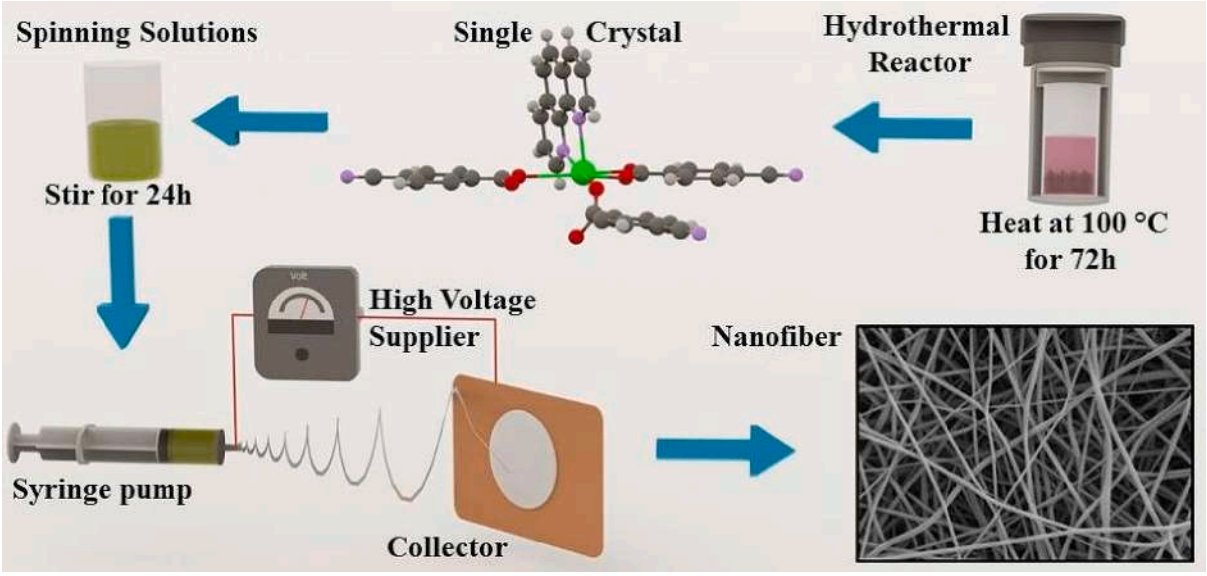

Scheme 1. Schematic presentation of the preparation of Ho@PVP and Yb@PVP nanofibers.

most organic solvents, further adding to its appeal and versatility [26–30].

To the best of our knowledge, while numerous studies have explored the impact of various organic/inorganic dopants on the structural, electrical, and optical properties of PVP composite materials, limited research has been studied on the doping effect of rare earth ions. For instance, *Li et al.* demonstrated that a low content of $Eu(TFI)_3TPPO$, ensuring proper dispersion within the PVP matrix, yielded significantly higher luminescence efficiency compared to pure $Eu(TFI)_3TPPO$ [31]. *Zhang et al.* demonstrated the preparation of $Ag@SiO_2@Eu(tta)_3$-phenPVP nanoparticles using the electrospinning method. They found that the inclusion of PVP polymer created a favorable microenvironment that effectively stabilized the luminescent intensity of the $Ag@SiO_2@Eu(tta)_3phen$ composites [32]. In a study conducted by Verlan et al., they utilized chemical methods to prepare a $PVP/Eu(TTA)_2(Phen_3PO)_2NO_3$ nanocomposite. They indicated that this nanocomposite could create a relatively stable environment for lanthanide compounds, thereby enhancing their optical properties [33]. *Bai et al.*, $Eu_2(BTP)_3(H_2O)_4/PVP$ was produced using electrospinning. The research demonstrated that the PVP polymer matrix creates a stable chemical environment for Eu^{3+} compounds. The strong interaction between $Eu_2(BTP)_3(H_2O)_4$ and the PVP polymer matrix resulted in a significant enhancement in the luminescence intensity of $Eu_2(BTP)_3(H_2O)_4/PVP$ compared to $Eu_2(BTP)_3(H_2O)_4$ [34]. In our previous study, we utilized electrospinning to prepare composite fibers comprising $\{[Dy(2\text{-}stp)_2(H_2O)_6]0.2(4,4'\text{-}bipy)$ and $\{[Ho(2\text{-}stp)_2(H_2O)_6]0.2(4,4'\text{-}bipy)0.5(H_2O)\}$ compounds in PVP. Our findings revealed a substantial enhancement in both thermal stability and stable luminescence properties of the composite fibers compared to their pure compounds [35].

In this research, the photoactive composite fibers of $\{Ho(4cba)_3(phen)(H_2O)\}$@PVP and $\{Yb(4cba)_3(phen)\}$@PVP were fabricated by incorporating the coordination polymers (at 10, 15, and 20 wt%) into the polymer matrix of PVP, taking advantage of electrospinning. The photoluminescence properties of these 1D composite fibers were extensively examined at room temperature and low temperature, and their performance was compared to that of their pure compounds.

2. Experimental details

2.1. Materials and physical measurements

$HoCl_3{\cdot}6H_2O$ (99.9%, Sigma-Aldrich Co.), $YbCl_3{\cdot}6H_2O$(99.9%, Fluorochem Ltd.), 1,10-Phenanthroline monohydrate (≥99%, Sigma-Aldrich Co.), 4-Cyanobenzoic acid (99%, Fluorochem Ltd.), Polyvinylpyrrolidone (PVP, $M_w \sim 1{,}300{,}000$ by LS, from powder, Sigma-Aldrich Co.) and ethanol (99.8%, Sigma-Aldrich Co.) were purchased from Sigma-Aldrich Co. and FluorochemLtd. and used as taken without further purification. Elemental analysis was executed on an Elementar Vario-EL-III microanalyzer. FT-IR spectral data were measured on a Perkin Elmer Spectrum 65 spectrophotometer equipment with ATR-Kit system in the range of 4000–600 cm^{-1} at room temperature. Thermal stability was realized with a PerkinElmer TGA 4000 thermogravimetric analyzer. The SEM images were recorded using a FEI QUANTA 250 FEG, equipped with an energy-dispersive spectroscopy (EDX) system. The average diameter and the diameter size distribution of the composite fibers were obtained with Image J software from SEM images. The PL spectra were measured with an ANDOR SR500i-BL luminescence spectrometer equipped with a triple grating and detected by Intensified Charge Coupled Device (ICCD) camera as a detector for the visible region and InGaAs detector for NIR region. A frequency tripled Nd:YLFQ-switched pulse laser at 349 nm was used for the excitation source. Powder X-ray diffraction patterns were measured with a Philips PW-1710/00 diffractometer equipped with the Cu-Kα radiation (λ = 1.5418 Å) in the range $5° < 2\theta < 50°$ in the θ–θ mode with a n s step (5 s < n < 10 s) and a step width of 0.03°.

2.2. Synthesis of {[Ho(4cba)$_3$(phen)(H$_2$O)]} (1) and {[Yb(4cba)$_3$(phen)]} (2)

All the coordination polymers were synthesized the same as reported in the earlier method [36,37]. Solution A: the mixture of 4cba (0.147 g, 1.0 mmol) and phen (0.198 g, 1.0 mmol) in EtOH (10 mL) was prepared and Solution B: the mixture of $HoCl_3{\cdot}6H_2O$ (0.379 g, 1.0 mmol) for Ho (**1**), $YbCl_3{\cdot}6H_2O$ (0.387 g, 1.0 mmol) for Yb (**2**) and deionized water (10 mL) was added dropwise to the above solution A under stirring and was adjusted by NaOH (1 mol/L) with pH≈6, and the final mixed solution continuous stirring was for at least 3 h at room temperature and then was sealed in a Teflon-line autoclave and heated at 100 °C for 3 d. After cooling to ambient temperature, the reaction solution was filtered and washed with cold EtOH several times and then dried at ambient temperature. The resulting crystals of Ho (**1**) (Pink) and Yb (**2**) (yellow) crystals were obtained. Yield: 61% (based on Ho). Anal. calc. for $C_{72}H_{44}Ho_2N_{10}O_{14}$ (%): C 43.95, H 8.77, N 6.74; Found: C 43.92, H 8.79, N 6.71. Yield: 64% (based on Yb). Anal. calc. for $C_{72}H_{40}Yb_2N_{10}O_{12}$ (%):

Table 1
Crystal data and structure refinement information for Ho (**1**) and Yb (**2**).

	Ho (**1**)	Yb (**2**)
Chemical Formula	$C_{72}H_{44}Ho_2N_{10}O_{14}$	$C_{72}H_{40}Yb_2N_{10}O_{12}$
Formula w. (g mol^{-1})	1603.03	1583.22
Crystal system	Triclinic	Triclinic
Space group	*P*-1	*P*-1
Unit cell dimensions	a = 8.2353 (4) Å b = 12.7637 (6) Å c = 16.3563 (8)Å α = 98.033 (4)° β = 101.999 (4)° γ = 100.032 (4)°	a = 9.8939(3) Å b = 11.7425(5) Å c = 15.0486(6) Å α = 111.396(4)° β = 96.416(3)° γ = 101.250(3)°
V / Å^3	1628.12(14)	1564.20(11)
Z	1	1
ρ_{calc} / g cm^{-3}	1.635	1.681
μ/mm^{-1}	2.488	3.046
Temperature (*K*)	296	295
Reflections collected	8913	18,532
Independent reflections	6105 [R_{int} = 0.029]	6386 [R_{int} = 0.048]
S	1.029	1.040
R_1 [*I* > 2σ(*I*)]	0.0370	0.0299
wR_2 [*All Data*]	0.0630	0.0587

C 44.62, H 8.55, N 6.85; Found: C 44.58, H 8.58, N 6.81.

2.3. Preparation of spinning solutions

In a typical procedure, PVP was employed as the matrix material at a concentration of 15% (m/V) in the following steps: Briefly, 1,5 g of PVP was dissolved in 10 mL of EtOH solution, and the solution was stirred with a magnetic stirrer for homogeneity for 24 h at room temperature. Then, the different proportions of Ho (**1**) and Yb (**2**) compounds correspond to 5 wt%–25 wt% (5, 10, 15, 20 and 25 wt%) respectively were added to PVP and stirred for another 12 h at room temperature for homogeneity and transparency (Scheme 1).

2.4. Electrospinning process

Electrospinning was carried out in the laboratory spinning unit (SPINGENIX SG-1) under a 13.5 kV by a DC high-voltage generator in horizontal alignment. The spinning solutions mentioned above were ejected using 5 mL plastic injectors equipped with a non-rust steel needle having an inner diameter of 0.8 mm. A fluid supply rate was set at 2 mL/h and the distance between the collector and the needle tip was set at 20 cm. Randomly arranged nanofibers were assembled on an electrically grounded aluminum foil. Next, the composite fibers were placed in a vacuum-drying oven at 40 °C for 12 h to remove the residual organic solvent.

2.5. X-ray structure determination

Suitable single-crystals Ho (**1**) and Yb (**2**) compounds were selected for data collection and performed on a Rigaku-Oxford XCalibur X-ray diffractometer at Room Temperature with EOS-CCD detector using graphite-monochromated MoK_α radiation (λ = 0.71073 Å) with ω-scan mode. The processing of data was carried out in CrysAlis^{Pro} software. Crystal data collection, data reduction and analytical absorption corrections were accomplished using the CrysAlis^{Pro} software v. 1.171.41.93a [38,39]. Using Olex2 [40] as the graphical interface, the structures were solved by the ShelXS structure solution program, employing the Direct method [41]. The model was refined by full-matrix least-squares on F^2 in SHELXL [42]. All non-hydrogen atoms were refined anisotropically and hydrogen atoms were added to the structure in idealized positions and further refined according to the riding model. Geometrical calculations were performed using PLATON software [43] and molecular graphics were generated using OLEX2 version 1.2.8. Table 1 summarizes the processes of the data collection and refinement of these compounds. The selected bond lengths and angles of Ho (**1**) and Yb (**2**) were shown in Table 2 and the hydrogen-bond geometry and π–π interactions were illustrated in Table 3.

Table 2
Selected bond lengths (Å) and bond angles (°) of Ho (**1**) and Yb (**2**).

	1	**2**
Bond lengths		
Ln-O_w	2.370(3)	
Ln-O_{4cba}	2.278(3)-2.351(3)	2.231(2)-2.446(2)
Ln-N_{phen}	2.546(3)-2.566(4)	2.492(3)-2.558(3)
Bond Angles		
O_w-Ln-$O4_{cba}$	72.91(12)-143.23(12)	
O_w-Ln-N_{phen}	73.61(12)-117.34(12)	
$O4_{cba}$-Ln-O_{4cba}	72.83(9)-145.56(10)	54.69(8)-147.61(9)
$O4_{cba}$-Ln-N_{phen}	68.83(11)-147.63(11)	71.25(8)-143.38(9)
N_{phen}-Ln-N_{phen}	63.96(13)	65.11(9)

Table 3
Hydrogen-bond geometry (Å,°).

	D – H···A[a]	**D – H**	**H···A**	**D···A**	**D – H···A**	**Symmetry**
1	O(1) – H(1B) ···O (7)	0.73 (5)	2.14 (5)	2.815 (5)	154	1 + x,y,z
	C(26) – H(26) ···N (1)	0.93 (3)	2.57 (3)	3.408 (7)	150	1-x,1-y,-z
2	C(35) – H(35) ···O (2)	0.93 (3)	2.41 (5)	3.183 (5)	126	2-x,2-y,1-z
	Cg(I)···Cg(J)			Cg··· Cg		
	Cg(1)···Cg(1)			4.724 (3)		1-x,1-y,1-z
	Cg(1)···Cg(2)			4.708 (3)		2-x,1-y,1-z
	Cg(1)···Cg(6)			3.815 (3)		1-x,1-y,1-z
1	Cg(2)···Cg(2)			4.741 (3)		2-x,1-y,1-z
	Cg(2)···Cg(6)			3.658 (3)		2-x,1-y,1-z
	Cg(3)···Cg(4)			4.788 (3)		−1 + x,y,z
	Cg(4)···Cg(5)			3.974 (3)		1-x,-y,1-z
	Cg(6)···Cg(6)			4.274 (3)		1-x,1-y,1-z
	Cg(1)···Cg(1)			3.707 (2)		1-x,1-y,1-z
	Cg(1)···Cg(6)			3.930 (3)		1-x,1-y,1-z
2	Cg(2)···Cg(5)			4.988 (2)		1 + x,y,z
	Cg(3)···Cg(5)			4.294 (3)		1 + x,y,z

[a] D: Donor, A: Acceptor, Cg(I): Plane Number I (=ring number in () above), Cg (1): N(4) –C(25) – C(26) – C(27) – C(28) – C(29); Cg(2): N(5) – C(30) – C(31) – C (34) – C(35) – C(36); Cg(3): C(2) – C(3) – C(4) – C(5) – C(6) – C(7); Cg(4): C(10) – C(11) –C(12) – C(13) – C(14) – C(15); Cg(5): C(18) – C(19) – C(20) – C(21) – C (22) – C(23); Cg(6): C(28) – C(29) – C(30) – C(31) – C(32) – C(33).

3. Results and discussion

3.1. Crystal structure

The single-crystal data derived from X-ray diffraction analysis shows that Ho (**1**) and Yb (**2**) are isostructural, crystallized in a triclinic system, *P*-1 space group, so we will explain Ho (**1**) for detailed structural discussions.

3.2. {[Ho(4cba)$_3$(phen)(H$_2$O)]} (1)

Single-crystal X-ray diffraction studies reveal that the crystal of Ho

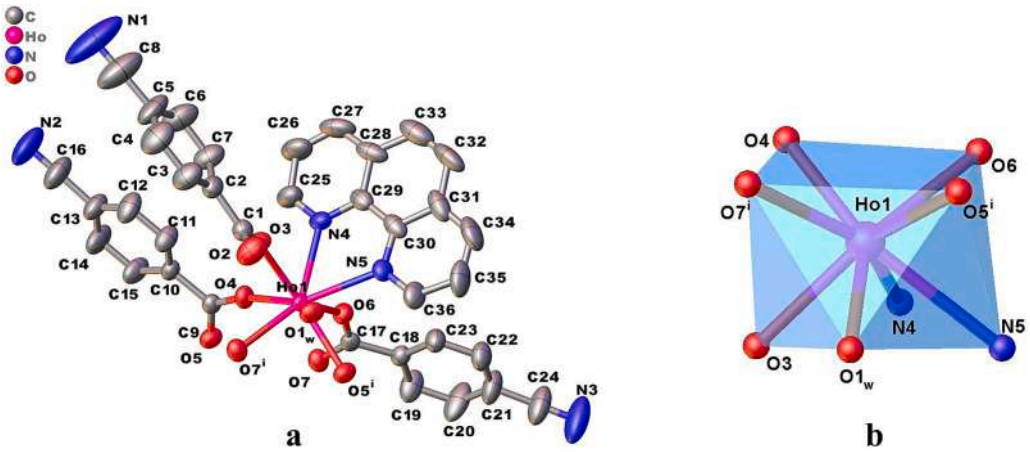

Fig. 1. Representation of the molecular structure and coordination environment of Ho (**1**) (The hydrogen atoms were omitted for clarity).

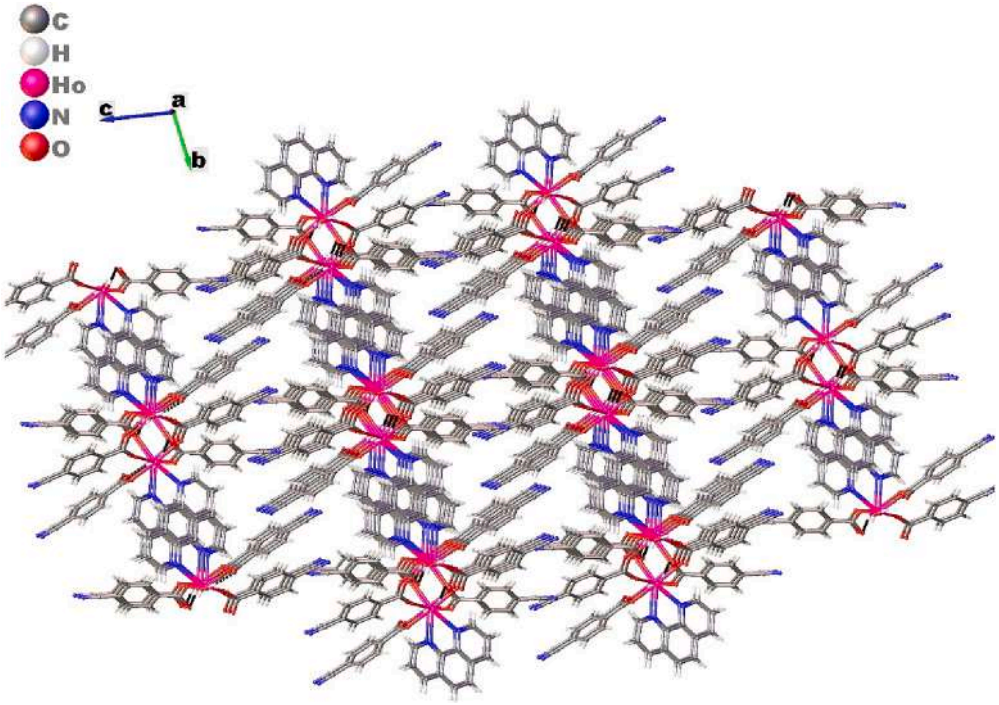

Fig. 2. A view of the 1D hydrogen-bonded of Ho (**1**), which is extended to an infinite chain along with the *a*-axis.

(**1**) contains a center-related dinuclear $[Ho_2(CO_2)_4]$ unit (Fig. 1a). The four carboxylate groups link a pair of Ho^{3+} atoms with $Ho^{3+}\cdots Ho^{3+}$ distances of 4.401(9) Å, together in the CO_2-bridging mode, produce a paddle-wheel-like centrosymmetric dimer. The Ho^{3+} atom is coordinated by four O atoms from four bridging 4cba ligands, one O atom from a monodentate 4-cba, two N atoms from one chelating phen molecule, and one coordinated water molecule. These eight coordination atoms form a distorted square antiprism (Fig. 1b). The bond lengths of Ho–O and Ho–N range from 2.278(3)–2.370(3)Å and 2.546(3)–2.566(4)Å, respectively. The O–Ho–O/N bond angles are in the range of 68.83(11) to 147.63(11) and N–Ho–N bond angle is 63.96(13). All of the bond distances and bond angles are comparable to the reported Ho(**1**) compounds [44–46]. The carboxylate groups are bound to the Ho^{3+} ions in three different coordination modes: a bidentate bridging mode in the *syn*-syn configuration, a bidentate bridging coordination mode in the *syn*-anti configuration and a common monodentate mode. To the best of our knowledge, Yan Li et al. co-workers have studied Ln^{3+}(4cba)(phen)-like compounds [47] Sheybani et al. have studied fluoro-bridged Ho^{3+}(FBA)$_3$(2,2′-bipy) Metal – Organic Frameworks. According to this research, 2-FBA ions were bounded to the RE metal ions. As the organic linker H_3BTB, which is in DMF, was modulated in a fluoro-bridged nonanuclear and trinuclear cluster MOF [48].

Meanwhile, the hydrogen bonds and π–π stacking interactions play an important role in the crystal packing and stabilization of Ho (**1**). Between the uncoordinated carboxylate O atom and the coordinated water molecule have been observed hydrogen bonding interactions, forming generate a 1D chained network along *a*-direction (Fig. 2). It is also surprising that in Ho (**1**), π–π stacking interactions exist 4cba-4cba, 4cba-phen and phen-phen molecule rings, with the centroid-to centroid distances in the range of 3.974–4.788, 3.658–3.815 and 4.708–4.741 Å, respectively. These interactions help in strong layer packing and stabilizing the framework structure. The strong packing of the layers stabilized the layers and resulted in a permanent two-dimensional (2D) network parallel to the bc-plane (Fig. 3)[49,50].

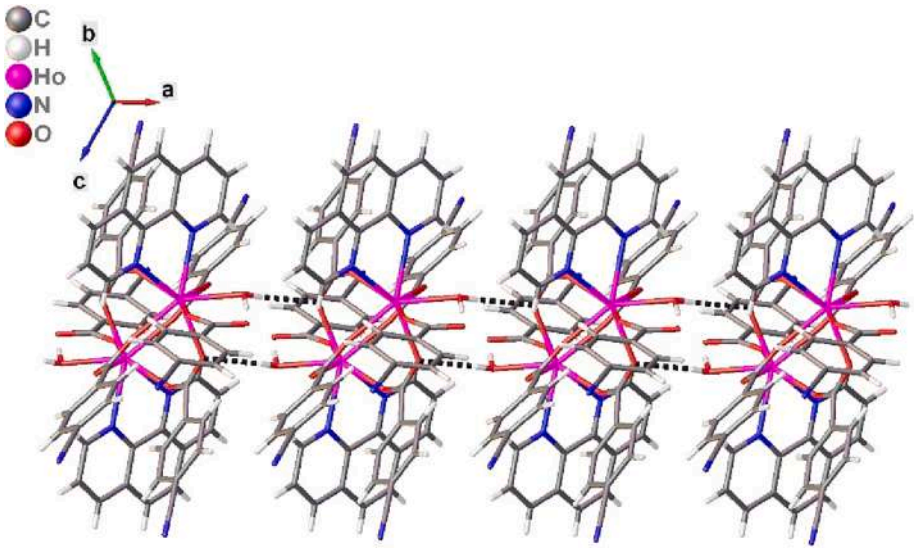

Fig. 3. Projection view of the 2D molecular network parallel to the *bc*-plane of Ho (**1**).

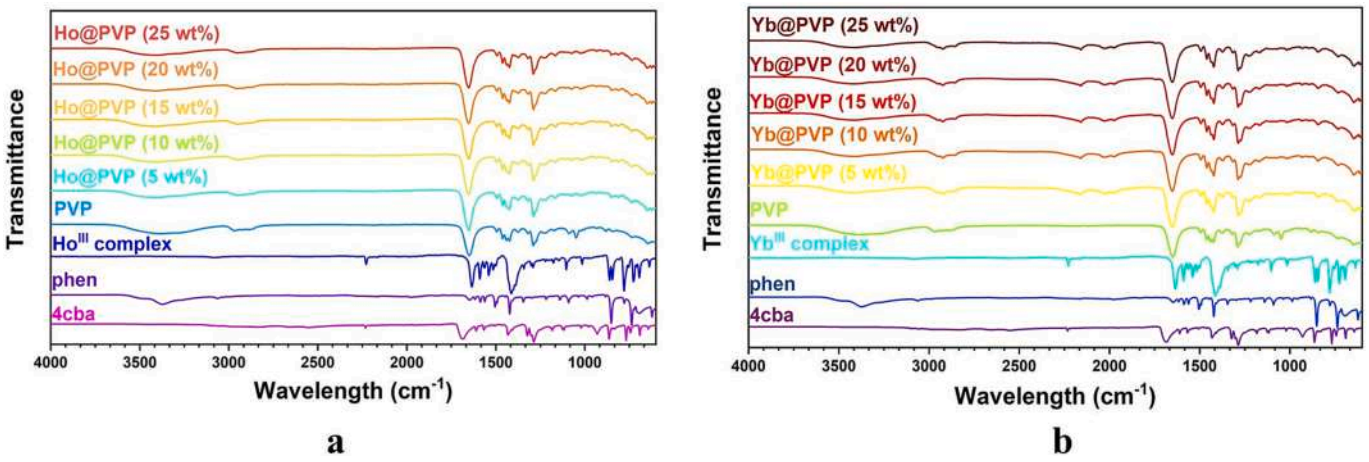

Fig. 4. FT-IR spectra of 4cba, phen and PVP (a) Ho (**1**) and Ho@PVP, (b) Yb (**2**) and Yb@PVP.

3.3. Powder X-ray diffraction and FTIR analysis

The PXRD measures of synthesized compounds give important information about purity. The powder X-ray diffraction (XRD) patterns of Ho (**1**) and Yb (**2**) match well with those of simulated patterns (Fig. S1, see the SI). It is hence concluded that the phase purity of the two compounds is high.

To understand bond characteristics and chemical bond formations between the dopant and host polymer the Ho@PVP and Yb@PVP fibers (5 wt%–25 wt%), pure compounds and their precursors were analyzed by FTIR (Fig. 4). In general, the compounds and their nanofibers exhibited almost identical behavior in all spectra. Therefore, Ho (**1**), along with its fibers and free ligands, will be discussed in detail as representative examples. The FT-IR spectrum of Ho (**1**) revealed characteristic absorption peaks of its organic ligands, 4cba and phen, in closely located regions. However, notable differences were observed between the IR spectra of the compounds and the free ligands. The cyano ν(C≡N) stretching vibration is observed at a similar frequency of approximately 2228 cm^{-1}, which is consistent with the absorption peak observed for the free 4-Hcba ligand. This indicates that the cyano group is not involved in coordination. The carboxylate vibration's out-of-plane bending vibration, δ(O—H), observed at 928 cm^{-1} in the free 4-Hcba ligand, disappears upon the formation of the compounds. This phenomenon can be attributed to the presence of intramolecular hydrogen bonding. One noteworthy feature observed in the IR spectra of the investigated compounds is the stretching vibration, ν(COO), of the carboxylate group. The asymmetrical stretching frequency, ν_{asym}(COO), of Ho (**1**) at 1637 cm^{-1} closely resembles that of the free 4-Hcba ligand (1689 cm^{-1}) due to the presence of a short C—O bond. On the other hand, the symmetrical stretching frequency, ν_{sym}(COO), around 1409 cm^{-1} aligns with the presence of the COO^- ion [51]. The weak absorption band observed in the range of 3052–3085 cm^{-1} can be attributed to the ν(C—H) vibration, likely originating from the phen ligand [52]. The spectrum of Phen exhibits two peaks at 851 cm^{-1} and 732 cm^{-1}, corresponding to the out-of-plane bending vibration of C—H, as well as two peaks at 1500 cm^{-1} and 1414 cm^{-1}, corresponding to the stretching vibration modes of C=N and C—N. In the spectra of Ho (**1**), these peaks are slightly shifted, indicating the involvement of the Ho^{3+} -N stretching vibration [53–55]. Furthermore, the pure PVP polymer matrix exhibits four additional characteristic absorption bands. The asymmetrical stretching of CH_2 and the bending of CH_2 in the polymer backbone were detected at 2971 cm^{-1} and 1428 cm^{-1}, respectively, which are indicative of the PVP polymer matrix. A strong stretching band corresponding to carbonyl (C=O) was observed at 1660 cm^{-1}. Additionally, a vibration band at 1287 cm^{-1} was observed, attributed to the stretching of (C—N) bonds. It was observed that all composite samples (Ho@PVP) containing

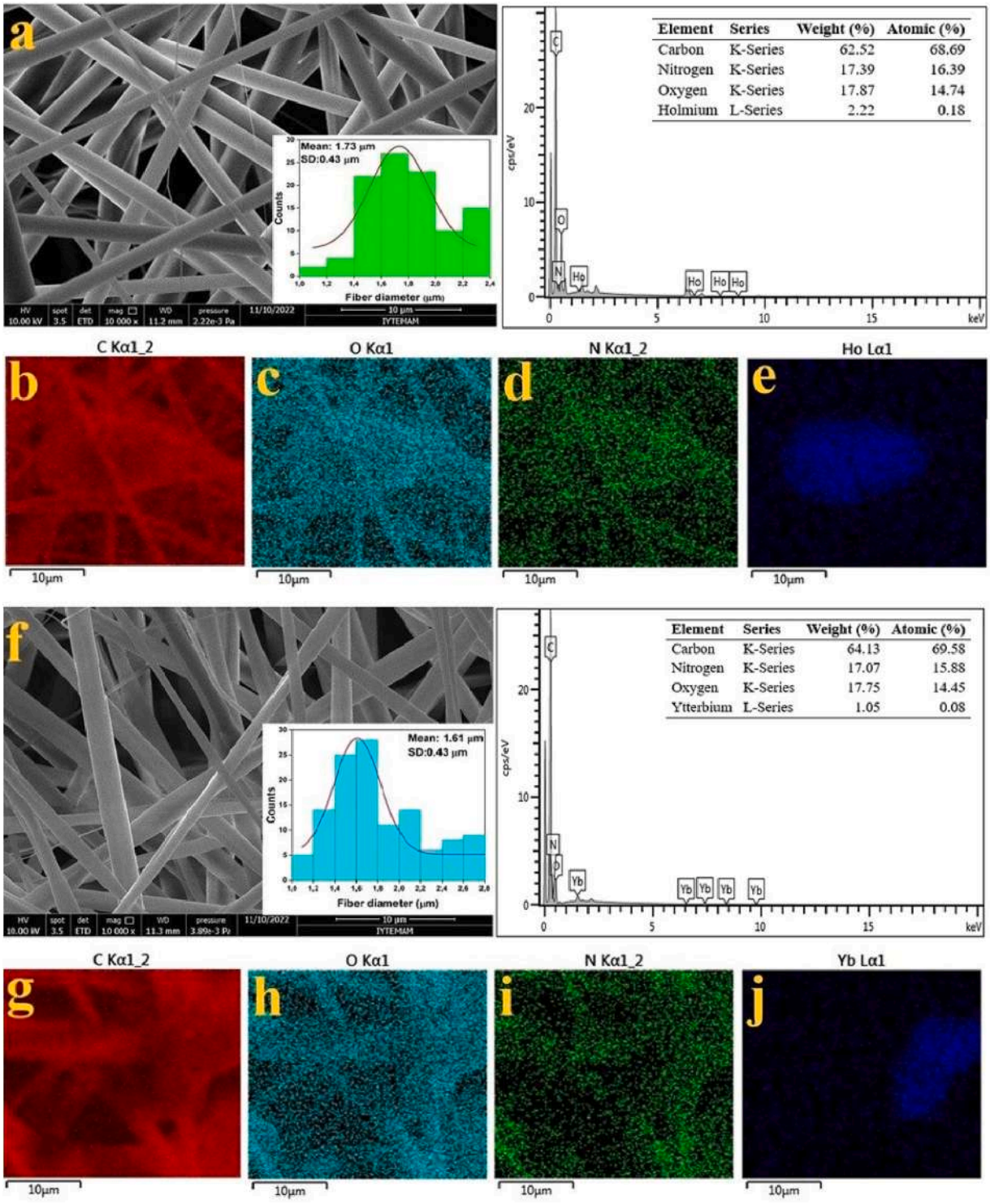

Fig. 5. A) sem images and size distribution and edx of optimized of Ho@PVP (20 wt%) and elemental mapping of the b) carbon (C), c) oxygen (O), d) nitrogen (N), e) holmium (Ho) and f) SEM images and size distribution and EDX of optimized of Yb@PVP (15 wt%), g)carbon (C), h) oxygen (O), i) nitrogen (N), j) ytterbium (Yb).

PVP exhibited a consistent IR band. Furthermore, the distinctive band of PVP at 1660 cm^{-1}, corresponding to the stretching band of C═O, was found to be slightly shifted to a lower wavenumber (1654–1650 cm^{-1}). This shift indicates the effective doping of Ho^{3+} compound within the PVP polymer matrix [35,56].

3.4. Morphology of analysis of composite fibers

The SEM was used to examine the surface morphology of the electrospun products Ho@PVP and Yb@PVP, which contained varying concentrations of Ho (**1**) and Yb (**2**) compounds, in order to investigate their surface morphology. Figures 5 and S2(see the SI) display SEM micrographs and histograms of the Ho@PVP and Yb@PVP, respectively. The bottom-right inset of Fig. 5 and Figure S2 displays the histogram figures, showing the fiber diameters and their corresponding standard deviations in the SEM images. The average diameters of 1D composite fibers increased from 1.09 ± 0.39 µm (5 wt%) to 1.98 ± 1.09 µm (25 wt %) for Ho@PVP and 1.29 ± 0.52 µm (5 wt%) to 2.09 ± 0.79 µm (25 wt

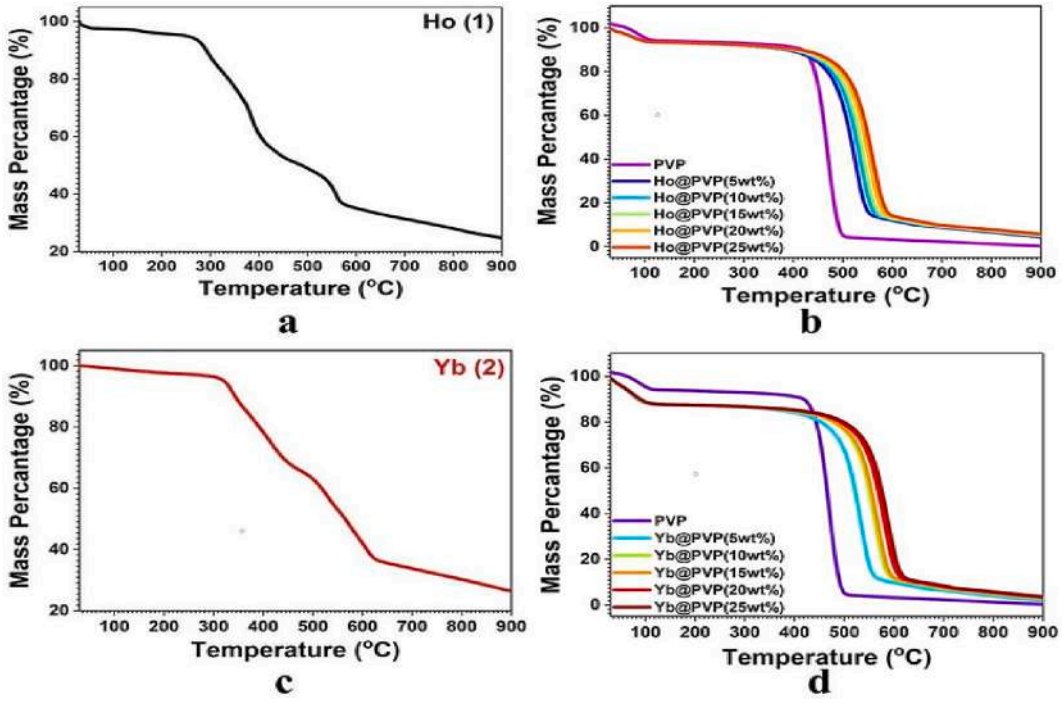

Fig. 6. TGA curve of (a) Ho (**1**), (b) Ho@PVP, (c) Yb (**2**), (d) Yb@PVP.

%) for Yb@PVP, respectively. According to the SEM histograms, the incorporation of Ho (**1**) and Yb (**2**) compounds into the PVP matrix increased the viscosity of the solutions and improved the electrical conductivity of the soluble materials. This increase in viscosity and conductivity led to the aggregation of fibers during the electrospinning process, resulting in larger fiber diameters [57]. SEM images of Ho@PVP and Yb@PVP composite fibers have provided almost nearly smooth surfaces, while a few fibers with relatively irregular and rough. Thus, the successful combination of Ho (**1**), Yb (**2**) compound and PVP polymer matrix was affirmed by the increase in the diameter of the

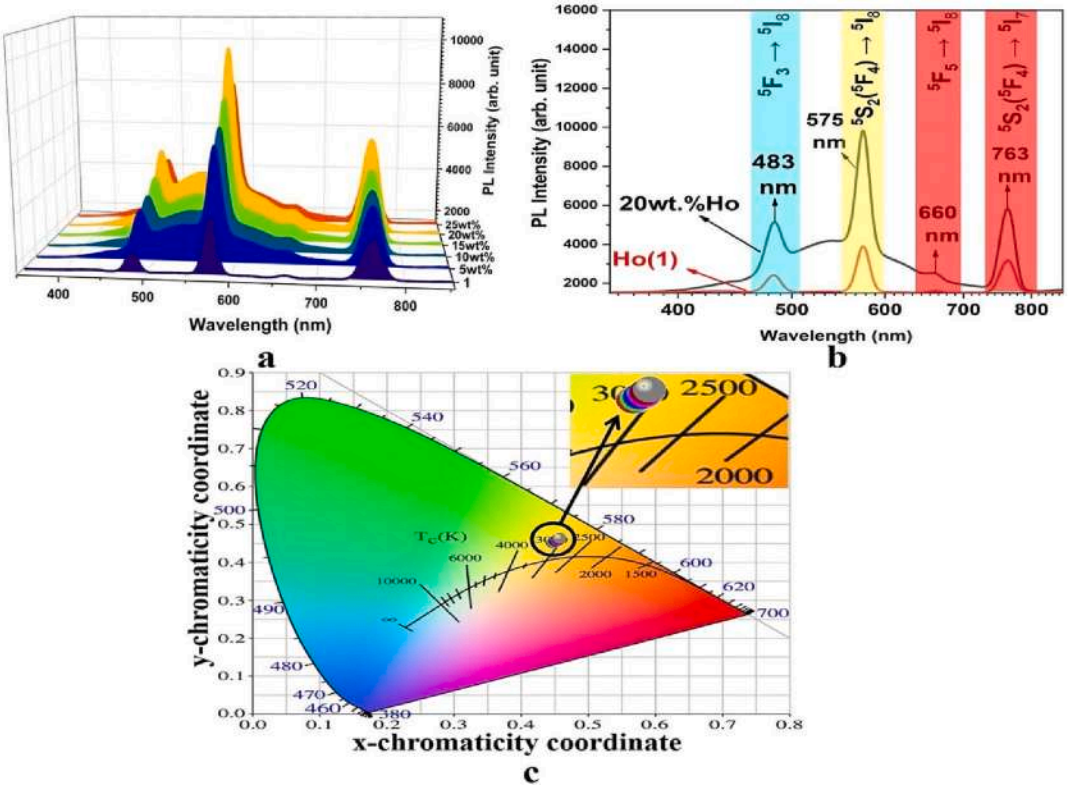

Fig. 7. The solid-state PL spectra of (a) Ho (**1**) and Ho@PVP composite fibers (5 wt% – 25 wt%) at room temperature (λ_{exc} = 349 nm), (b) Ho (**1**) and Ho@PVP composite fiber (20 wt%) with the possible 4f-4f transition. (c) Chromaticity coordinates of Ho (**1**) and Ho@PVP composite fiber.

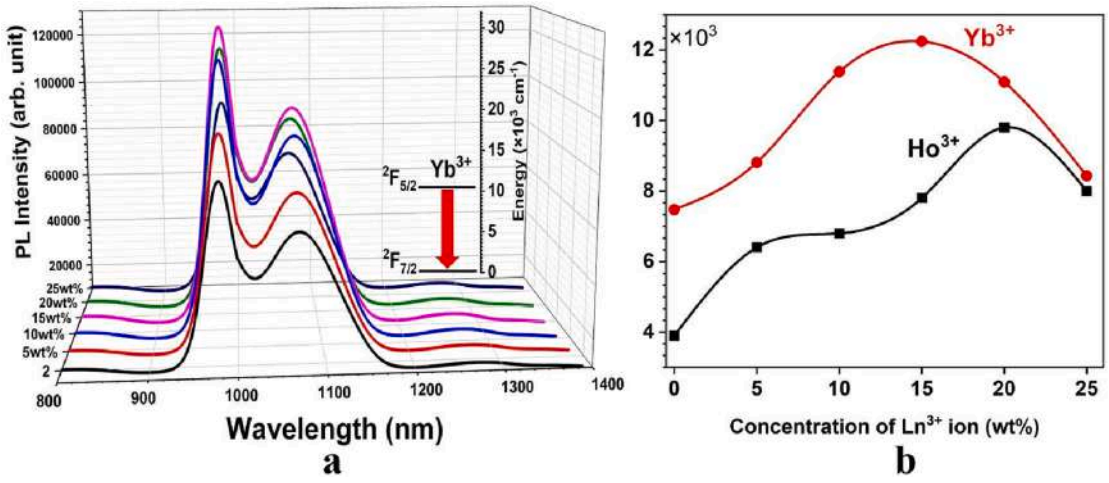

Fig. 8. (a) The solid-state PL spectra of Yb (**2**) and Yb@PVP composite fibers (5 wt%-25 wt%) at room temperature (λ_{exc} = 349 nm), (b) The dependence of compounds and their composite fibers emission intensity as a function of the Ho^{3+}/Yb^{3+} content.

composite fiber, which was proved in the SEM images. As a result, the doped Ho (**1**) and Yb (**2**) compounds are uniformly distributed around the fiber in the PVP matrix, recommending that it may be well compatible with PVP.

Energy dispersive X-ray spectroscopy (EDX) is a commonly used technique for determining the elemental composition of a specific region within a sample. In this study, EDX was employed to confirm the homogeneous synthesis of Ho@PVP and Yb@PVP composite fibers. During the EDX analysis, specific regions of interest were examined, revealing peaks that correspond to the elements present in the host materials. The EDX results provided confirmation that the as-electrospun products consisted of C, O, N and the respective elements Ho (for Ho (**1**)) or Yb (for Yb (**2**)). The successful incorporation of Ho (**1**) and Yb (**2**) into the PVP matrix was clearly observed in the EDX spectrum, as depicted in Fig. 5. The prominent peaks corresponding to the elements present within the region of interest were identified. The atomic and weight percentages of the composite fibers were determined and are summarized in the inset table of the EDX graph shown in Fig. 5. The presence of similar peaks in the spectrum indicates the formation of stable fibers with the correct atomic distribution, which is essential for subsequent optical and structural investigations [58]. Furthermore, these results provide support for the luminescence and structural analyses [59].

3.5. TGA analysis

TGA is a common thermal analysis technique that is particularly useful for observing the thermal decomposition of organic–inorganic hybrid materials [60,61]. TGA of all samples was performed under a nitrogen atmosphere in the temperature range of room temperature to 900 °C. Fig. 6 represents the TGA curves for the pure Ho (**1**) and Yb (**2**) compounds, pure PVP and their composite fibers. The results show that pure Ho/Yb compounds indicate almost similar thermal behaviours and exhibit several steps of weight loss. Ho (**1**) compound, the weight loss of 3.1% was observed from room temperature to 150 °C, corresponding to the loss of one coordination water molecule and the structure is thermally stable from 150 to 325 °C. As for Yb (**2**), it is immediately apparent that Yb (**2**) compound is thermally stable up to 325 °C. Both compounds undergo dramatic weight loss (Ho (**1**) 63.3% and Yb (**2**) 63.9%) in the temperature range of 325–620 °C, which could be attributed to the ligand decomposition and the coordination polymer framework beginning to collapse. As a result, we speculate that the final residual weight likely originated from Ho^{3+}/Yb^{3+} oxide [44,62].

As for the PVP matrix and Ho/Yb@PVP composite fibers, all samples have similar thermal properties. The TGA graphs show two-step weight loss patterns for the polymer fibers, which is the normal decomposition behaviour of PVP. At the preliminary stage of the phenomenon, the reduction of weight is initiated, which is due to the evaporation of water and environmental humidity. The second loss of mass in the samples occurred a drastic decrease at 350 °C, which is due to the degradation of the molecules' large chains into small fragments and the weak head-to-head linkage at the terminal end. Moreover, the constant loss of weight noticed between 344 and 501 °C is due to the degradation of the PVP chains. However, with the addition of Ho (**1**) and Yb (**2**) compounds in the PVP matrix, where show degradation shifts to higher temperature degrees, which is attributed to the arrangement of polymeric chains near the compounds, which can raise heat dissipation. Ho@PVP and Yb@PVP composite fibers have increased thermal stability with an increase in the Ho/Yb concentration [63–65].

3.6. Photoluminescence properties

Solid-State PL spectra of the free ligands (4cba and phen), PVP, Ho (**1**) and Yb (**2**) compounds as well as their composite fibers (Ho@PVP and Yb@PVP), were examined at room temperature using UV laser excitation at 349 nm in the visible and/or near-infrared (NIR) regions. The results are presented in Fig. S3, Fig. 7 and Fig. 8. The free ligand 4cba exhibits indigo emission at 452 nm, accompanied by a minor shoulder attached to a broad band at 565 nm. On the other hand, the free ligand phen and the PVP polymer demonstrate a wide emission band at λ_{max} = 440 and 497 nm, corresponding to blue light emission. These emissions can be attributed to the electronic transition of the n-π* or π-π* (ILCT) [52,66–69].

The PL spectrum of Ho (**1**) exhibits four distinct peaks centered at 483, 575, 680, and 763 nm. These peaks correspond to the transitions $^5F_3 \rightarrow {}^5I_8$, $^5S_2(^5F_4) \rightarrow {}^5I_8$, $^5F_5 \rightarrow {}^5I_8$ and $^5S_2(^5F_4) \rightarrow {}^5I_7$ of the Ho^{3+} ion, respectively (Fig. 7b). Among these peaks, the yellow emission peak at 575 nm ($^5S_2(^5F_4) \rightarrow {}^5I_8$) displays a sharp and intense profile compared to the green emission peak at 483 nm ($^5F_3 \rightarrow {}^5I_8$) and the red emission peak at 680 nm ($^5F_5 \rightarrow {}^5I_8$). Consequently, the Ho (**1**) compound emits yellow light [70,71]. The PL spectra of Yb (**2**) are observed in the near-infrared (NIR) region, specifically at 980 nm ($^2F_{5/2} \rightarrow {}^2F_{7/2}$), with a shoulder peak at 1070 nm (Fig. 7d) [72]. Yb (**2**) possesses the $^2F_{5/2}$ state as its single excited state, which leads to luminescence through a spin-allowed transition of $^2F_{5/2} \rightarrow {}^2F_{7/2}$. The excited electrons transition from the split and energy-enhanced emissive state ($^2F_{5/2}$) to the ground state ($^2F_{7/2}$), resulting in the emission band at higher wavelengths (in the range of 980–1100 nm). The luminescent behavior is influenced by the ligand-field around the Yb^{3+} ion, which causes crystal splitting and consequently leads to a broad emission spectrum.

Based on the observations presented in Fig. 7a, Fig. 8a, and Fig. 8b,

Table 4
The CIE coordinates and CCT values of Ho (**1**) and Ho@PVP composite fibers (5 wt%-25 wt%).

Ho@PVP(xHo wt.%)	CIE chromaticity coordinates (x,y)		CCT value (K)
Ho(**1**)	0.449	0.454	3173.44
Ho@PVP (5 wt%)	0.451	0.456	3156.58
Ho@PVP (10 wt%)	0.453	0.458	3140.71
Ho@PVP (15 wt%)	0.456	0.460	3110.22
Ho@PVP (20 wt%)	0.457	0.463	3115.42
Ho@PVP (25 wt%)	0.459	0.466	3106.26

the PL emission intensities reach their maximum at a doping concentration of 20 wt% for Ho (**1**) and 15 wt% for Yb (**2**). The subsequent decrease in intensities at higher concentrations of Ho^{3+} and Yb^{3+} can be attributed to a phenomenon known as concentration quenching. This phenomenon is characterized by a high rate of cross-relaxation between luminescent centers, as well as energy transfer to hydroxyl-like ions, defect structures, and other exchange interactions. These non-radiative processes contribute to the decrease in the PL emission intensity [73–75].

The chromaticity coordinates of the Ho (**1**) and its composite fibers (5 wt%-25 wt%) were determined using the emission data shown in Fig. 7c and the calculated CIE values in Table 4, following the guidelines of the Commission Internationale de l'Eclairage (CIE). The calculated CIE chromaticity coordinates for the optimized composite fiber are x = 0.457 and y = 0.463. The correlation color temperature (CCT) values were calculated using McCamy's empirical formula (equation 1) [76]. CCT serves as a measure of the quality of a light source and provides an indication of whether the light appears cool, neutral, or warm in nature.

$$CCT = -449n^3 + 3525n^2 - 6823.3n + 5520 \quad (1)$$

where, the slope line (n) is defined as $n=(x-x_e)/(y-y_e)$, where × and y represent the CIE coordinates, and the chromaticity epicenters are given as $x_e = 0.332$ and $y_e = 0.185$. In general, when the correlated color temperature (CCT) of a lamp is above 4000 K, it is perceived to emit cool light, whereas a CCT below 3200 K is associated with warm light. The calculated CCT values are provided in Table 4. Considering the given

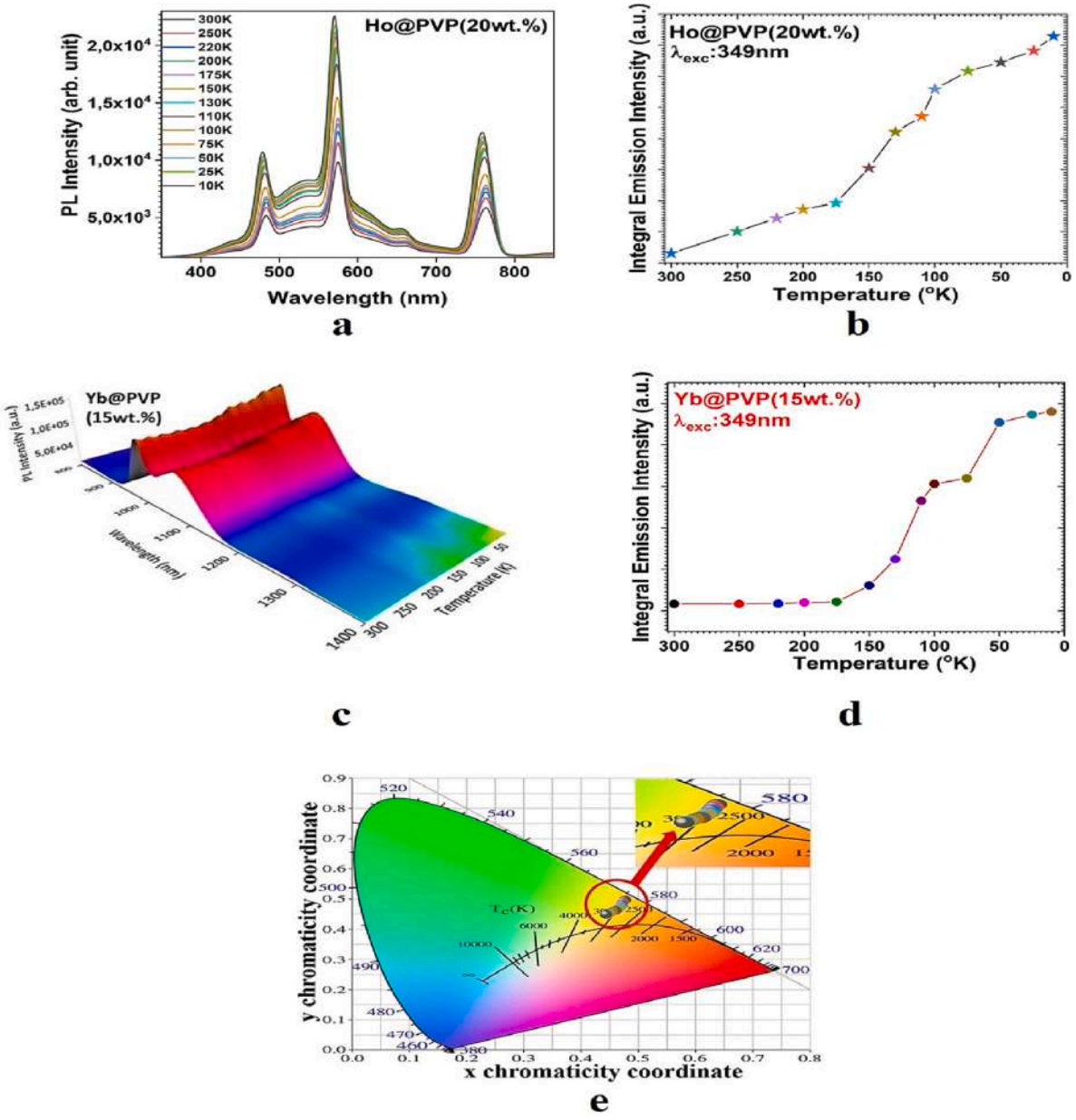

Fig. 9. Low-Temperature PL spectra of (a) Ho@PVP (20 wt%) and (c) Yb@PVP (15 wt%), the integral emission profiles of (b) Ho@PVP (20 wt%) and (d) Yb@PVP (15 wt%), (e) the chromaticity coordinates of the Ho@PVP (20 wt%) for the low-temperature analysis (λ_{exc} = 349 nm).

Table 5
The CIE coordinates and CCT values of Ho@PVP (20 wt%) composite fiber at low temperature.

Temperature(K)	CIE chromaticity coordinates (x,y)		CCT value(K)
10	0.489	0.509	2984.21
25	0.486	0.503	2985.66
50	0.484	0.496	2968.27
75	0.482	0.488	2945.46
100	0.479	0.486	2969.04
110	0.478	0.481	2952.37
130	0.474	0.478	2983.57
150	0.473	0.475	2977.06
175	0.467	0.472	3036.33
200	0.464	0.469	3057.32
220	0.461	0.468	3091.81
250	0.459	0.464	3094.74
300	0.457	0.463	3115.42

information, it can be observed that the color coordinates (x, y) for all Ho@PVP composite fibers fall within the yellow region. The low CCT values and the positioning of the color coordinates validate the potential of the prepared hybrid materials to be regarded as promising yellow luminescent materials [77–79].

3.6.1. Luminescence temperature quenching behavior of composite fibers

Temperature-dependent photoluminescence (PL) analysis plays a crucial role in understanding the optical properties of materials. Low-temperature measurements are particularly significant as they reveal spectral details that may not be apparent at room temperature due to thermal expansion effects. At cryogenic temperatures, electronic transitions from the ground state to different vibrational levels result in the emergence of excited states, allowing for the observation of fine structures in the PL spectra [80]. Given the significance of this analysis, the temperature-dependent PL spectra were recorded for Ho@PVP (20 wt%) and Yb@PVP (15 wt%) composites across a temperature range of 300–10 K. The corresponding spectra can be seen in Fig. 9(a-d). As depicted in the Figures, the intensity of the characteristic emission peaks of Ho@PVP and Yb@PVP exhibits a gradual decrease with the rise in temperature, which can be attributed to thermal quenching. It is worth mentioning that no new spectral bands associated with singlet radiative transitions were observed at low temperatures. This observation is likely attributed to the low thermal activation barrier for singlet–singlet non-radiative transitions [81,82]. Additionally, to investigate the impact of temperature on the emission color of the Ho@PVP (20 wt%) composite fiber, the CIE coordinates were calculated using the temperature-dependent emission spectra and plotted on the CIE chromaticity diagram (Fig. 9e). The emission color of the composite fiber was found to be minimally affected by temperature. The correlation color temperatures (CCT) values, calculated using McCamy's empirical formula, along with the chromaticity coordinates, are presented in Table 5 [83].

4. Conclusion

In summary, new Ho@PVP and Yb@PVP composite fibers were prepared by electrospinning, which demonstrated intense photoluminescence under ultraviolet excitation. The diameters of the composite fibers were increased in the range of 1.09–2.09 μm by changing the concentrations of Ho (**1**) and Yb (**2**). Owing to incorporating a polymer with good mechanical strength, thermal-stability and high dielectric constant desirable for electrospinning, the thermal and photostability of the composite nanofibers were much better than those of the pure compounds. The PVP polymer provides a rigid environment to protect the pure Ho/Yb compounds from decomposing under UV irradiation and high temperature. It is found that the PL spectra of the Ho@PVP composite fibers exhibit intense characteristic emissions from the Ho^{+3} ion, resulting in the emission of yellow light. The low CCT values and the positioning of the color coordinates affirm the potential of Ho@PVP hybrid materials as promising yellow luminescent materials. Furthermore, the Yb@PVP composite fibers demonstrate intense characteristic emissions from the Yb^{+3} ion in the NIR region, specifically at 980 nm with a shoulder peak at 1070 nm [84–87]. The PVP-supported hybrid materials possess high thermal stability and good film-forming properties, while the efficient Yb^{3+}-centered NIR luminescence opens up new possibilities for hybrid materials in future optoelectronic device applications.

CRediT authorship contribution statement

Fatma Kuru: Software, Conceptualization, Methodology. **Mustafa Burak Coban:** Writing – original draft, Writing – review & editing. **Ugur Erkarslan:** Visualization, Methodology. **Adem Donmez:** Software, Visualization. **Gorkem Oylumluoglu:** Software, Visualization. **Muhittin Aygun:** Software. **Hulya Kara Subasat:** Writing – review & editing.

Declaration of Competing Interest

The authors declare that they have no known competing financial interests or personal relationships that could have appeared to influence the work reported in this paper.

Data availability

Data will be made available on request.

Acknowledgements

The authors are grateful to the Research Funds of Balikesir University (BAP-2019/078) for the financial support, Dokuz Eylul University for the use of the Agilent Xcalibur Eos diffractometer (purchased under University Research Grant No. 2010.KB.FEN.13) and Balikesir University, Science and Technology Application and Research Center (BUBTAM) for the use of the Photoluminescence Spectrometer.

Data availability.
Data will be made available on request.

Appendix A. Supplementary data

Supplementary data to this article can be found online at https://doi.org/10.1016/j.poly.2023.116492.

References

[1] T. Chuasaard, S. Thammakan, N. Semakul, T. Konno, A. Rujiwatra, Structure and photoluminescence of two-dimensional lanthanide coordination polymers of mixed phthalate and azobenzene dicarboxylate, J. Mol. Struct. 1251 (2022), 131940.
[2] J. Feng, H. Zhang, Hybrid materials based on lanthanide organic complexes: a review, Chem. Soc. Rev. 42 (1) (2013) 387–410.
[3] J. Sun, Y. Xi, L. Gao, M. Hu, W. Liu, E. Ma, R. Huang, W. Qin, G. Wu, Two isostructural Ln-MOFs containing triazole groups as luminescent probes for efficient sensing of NACs and Fe3+, Inorganica Chim. Acta. 547 (2023), 121376.
[4] C. Zhang, S. Wei, L. Sun, F. Xu, P. Huang, H. Peng, Synthesis, structure and photocatalysis properties of two 3D Isostructural Ln (III)-MOFs based 2,6-Pyridinedicarboxylic acid, J. Mater. Sci. Technol. 34 (9) (2018) 1526–1531.
[5] M.-X. Wu, Y.-W. Yang, A fluorescent pillarene coordination polymer, Polym. Chem. 10 (23) (2019) 2980–2985.
[6] K. Panyarat, T.J. Prior, A. Rujiwatra, A series of new microporous lanthanide frameworks $[Ln(C_8H_3NO_6)(L)_{0.5}(H_2O)]\cdot 3H_2O$ (Ln=Pr,Nd,Sm and Gd, and L=$C_8H_4O_4$ or $C_8H_4O_4/C_8H_3NO_6$): Syntheses, characterization and photoluminescence properties, Polyhedron. 81 (2014) 74–80.
[7] S. Alghool, M.S. Zoromba, H.F.A. El-Halim, Lanthanide amino acid Schiff base complexes: synthesis, spectroscopic characterization, physical properties and in vitro antimicrobial studies, J. Rare Earths. 31 (2013) 715–721.
[8] B. Yan, Sol–gel preparation and luminescence of silica/polymer hybrid material incorporated with terbium complex, Mater. Lett. 57 (16-17) (2003) 2535–2539.
[9] K. Binnemans, Lanthanide-Based Luminescent Hybrid Materials, Chem. Rev. 109 (9) (2009) 4283–4374.
[10] Q. Xu, J. Tang, Y. Wang, J. Liu, X. Wang, Z. Huang, L. Huang, Y. Wang, W. Shen, L. A. Belfiore, Eu^{3+}-induced aggregates of diblock copolymers and their photoluminescent property, J. Colloid Interface Sci. 394 (2013) 630–638.

[11] A. Dwivedi, M. Srivastava, S.K. Srivastava, Ho^{3+}activated $Ca_{0.5}Y_{1.90-x}O_3$ green-emitting nanophosphors for solid state lightening: Synthesis, characterization and photoluminescence properties, J. Mol. Struct. (2022, 1251,), 132061.

[12] K. Yin, L. Zhang, C. Lai, L. Zhong, S. Smith, H. Fong, Z. Zhu, Photoluminescence anisotropy of uni-axially aligned electrospun conjugated polymer nanofibers of MEH-PPV and P3HT, J. Mater. Chem. 21 (2) (2011) 444–448.

[13] D. Paneva, F. Bougard, N. Manolova, P. Dubois, I. Rashkov, Novel electrospun poly (ε-caprolactone)-based bicomponent nanofibers possessing surface enriched in tertiary amino groups, Eur. Polym. J. 44 (3) (2008) 566–578.

[14] K. Naveen Kumar, K. Sivaiah, S. Buddhudu, Structural, thermal and optical properties of Tb^{3+}, Eu^{3+} and co-doped (Tb^{3+}+Eu^{3+}): PEO+PVP polymer films, J. Lumin. 147 (2014) 316–323.

[15] X. Liu, P.X. Ma, Phase separation, pore structure, and properties of nanofibrous gelatin scaffolds, Biomaterials. 30 (25) (2009) 4094–4103.

[16] M. Abrigo, S.L. McArthur, P. Kingshott, Electrospun Nanofibers as Dressings for Chronic Wound Care: Advances, Challenges, and Future Prospects, Macromol. Biosci. 14 (6) (2014) 772–792.

[17] Y. Gao, Y.i. Kuang, Z.-F. Guo, Z. Guo, I.J. Krauss, B. Xu, Enzyme-Instructed Molecular Self-assembly Confers Nanofibers and a Supramolecular Hydrogel of Taxol Derivative, J. Am. Chem. Soc. 131 (38) (2009) 13576–13577.

[18] S. Jiang, Y. Chen, G. Duan, C. Mei, A. Greiner, S. Agarwal, Electrospun nanofiber reinforced composites: a review, Polym. Chem. 9 (20) (2018) 2685–2720.

[19] B. Zaarour, L. Zhu, X. Jin, Controlling the surface structure, mechanical properties, crystallinity, and piezoelectric properties of electrospun PVDF nanofibers by maneuvering molecular weight, Soft Mater. 17 (2) (2019) 181–189.

[20] A.V. Stanishevsky, J.D. Wetuski, H. Yockell-Lelièvre, Crystallization and stability of electrospun ribbon- and cylinder-shaped tungsten oxide nanofibers, Ceram. Int. 42 (1) (2016) 388–395.

[21] P. Korycka, A. Mirek, K. Kramek-Romanowska, M. Grzeczkowicz, D. Lewińska, Effect of electrospinning process variables on the size of polymer fibers and bead-on-string structures established with a 2 3 factorial design, Beilstein J. Nanotechnol. 9 (2018) 2466–2478.

[22] B. Zaarour, L. Zhu, C. Huang, X. Jin, A mini review on the generation of crimped ultrathin fibers via electrospinning: Materials, strategies, and applications, Polym. Adv. Technol. 31 (2020) 1449–1462.

[23] M. Li, Z. Zhang, T. Cao, Y. Sun, P. Liang, C. Shao, Y. Liu, Electrospinning preparation and photoluminescence properties of poly (methyl methacrylate)/Eu^{3+} ions composite nanofibers and nanoribbons, Mater. Res. Bull. 47 (2) (2012) 321–327.

[24] V.S. Hingwe, K.A. Koparkar, N.S. Bajaj, S.K. Omanwar, Optical properties of one dimensional hybrid PVA/YVO4:Eu3+ nanofibers synthesized by electrospining, Optik (Stuttg). 140 (2017) 211–215.

[25] J. Li, J. Yan, G. Xue, J. Niu, Acoustic emission behavior of polyvinyl alcohol (PVA) fiber reinforced calcium sulphoaluminate cement mortar under flexural load, J. Build. Eng. 40 (2021), 102734.

[26] Q. Yang, Z. Li, Y. Hong, Y. Zhao, S. Qiu, C.e. Wang, Y. Wei, Influence of solvents on the formation of ultrathin uniform poly(vinyl pyrrolidone) nanofibers with electrospinning, J. Polym. Sci. Part B Polym. Phys. 42 (20) (2004) 3721–3726.

[27] D. Li, Y. Xia, Fabrication of Titania Nanofibers by Electrospinning, Nano Lett. 3 (4) (2003) 555–560.

[28] M.T. Hasan, R. Gonzalez, A.A. Munoz, L. Materon, J.G. Parsons, M. Alcoutlabi, Forcespun polyvinylpyrrolidone/copper and polyethylene oxide/copper composite fibers and their use as antibacterial agents, J. Appl. Polym. Sci. 139 (2022) 51773.

[29] A.B. Moghaddam, B. Shirvani, M.A. Aroon, T. Nazari, Physico-chemical properties of hybrid electrospun nanofibers containing polyvinylpyrrolidone (PVP), propolis and aloe vera, Mater. Res. Express. 5 (2018), 125404.

[30] M. Davidovich-Pinhas, S. Barbut, A.G. Marangoni, Physical structure and thermal behavior of ethylcellulose, Cellulose. 21 (5) (2014) 3243–3255.

[31] W. Li, Y. Tao, G. An, P. Yan, Y. Li, G. Li, One-dimensional luminescent composite nanofibers of $Eu(TFI)_3TPPO$/PVP prepared by electrospinning, Dye. Pigment. 146 (2017) 47–53.

[32] X. Zhang, J. Tang, H. Li, Y. Wang, X. Wang, Y. Wang, L. Huang, L.A. Belfiore, Red light emitting nano-PVP fibers that hybrid with $Ag@SiO_2@Eu(tta)_3$phen-NPs by electrostatic spinning method, Opt. Mater. (Amst) 78 (2018) 220–225.

[33] V.I. Verlan, M.S. Iovu, I. Culeac, Y. Nistor, C.I. Turta, V.E. Zubareva, Photoluminescence properties of PVP/$Eu(TTA)_2(Phen_3PO)_2NO_3$ nanocomposites, J. Non. Cryst. Solids. 357 (3) (2011) 1004–1007.

[34] J. Bai, H. Gu, Y. Hou, S. Wang, Luminescence properties and molecular mechanics calculation of bis-β-diketonate Eu^{3+} complex/polymer hybrid fibers, Opt. Mater. (Amst) 79 (2018) 310–316.

[35] M.B. Coban, E. Gungor, Y. Acar, F.K. Alpaslan, H.K. Subasat, Multifunctional Dy@PVP and Ho@PVP one-dimensional nanofibers: Electrospinning synthesis, luminescent and magnetic properties, J. Mol. Struct. 1272 (2023), 134117.

[36] Y. Acar, M.B. Coban, E. Gungor, H. Kara, Two New NIR Luminescencent Er(III) Coordination Polymers with Potential Application Optical Amplification Devices, J. Clust. Sci. 31 (1) (2020) 117–124.

[37] M.B. Coban, Hydrothermal synthesis, crystal structure, luminescent and magnetic properties of a new mononuclear Gd^{III} coordination complex, J. Mol. Struct. 1162 (2018) 109–116.

[38] CrysAlisPro Software, Version 1.171.41.93a, Rigaku Corporation, Oxford, UK, 2020.

[39] R.C. Clark, J.S. Reid, The analytical calculation of absorption in multifaceted crystals, Acta Crystallogr. Sect. A Found. Crystallogr. 51 (6) (1995) 887–897.

[40] O.V. Dolomanov, L.J. Bourhis, R.J. Gildea, J.A.K. Howard, H. Puschmann, OLEX2: a complete structure solution, refinement and analysis program, J. Appl. Crystallogr. 42 (2009) 339–341.

[41] G.M. Sheldrick, A short history of SHELX, Acta Crystallogr. Sect. A Found. Crystallogr. 64 (1) (2008) 112–122.

[42] G.M. Sheldrick, Crystal structure refinement with SHELXL, Acta Crystallogr. Sect. C, Struct. Chem. 71 (2015) 3–8.

[43] A.L. Spek, Structure validation in chemical crystallography, Acta Crystallogr. Sect. D Biol. Crystallogr. 65 (2) (2009) 148–155.

[44] M. Almáši, V. Zeleňák, L. Galdun, J. Kuchár, First 3D coordination polymer built from Ho(III) and 2-aminoterephthalate ligand, Inorg. Chem. Commun. 39 (2014) 39–42.

[45] G. Oylumluoglu, M.B. Coban, C. Kocak, M. Aygun, H. Kara, 2-and 1-D coordination polymers of Dy(III) and Ho(III) with near infrared and visible luminescence by efficient charge-transfer antenna ligand, J. Mol. Struct. 1146 (2017) 356–364.

[46] N.A. Ashashi, M. Kumar, R.M. Gomila, A. Frontera, H.N. Sheikh, S.C. Sahoo, Solvothermal synthesis and crystal structures of two Holmium(III)-5-Hydroxyisophthalate entangled coordination polymers and theoretical studies on the importance of π···π stacking interactions, J. Mol. Struct. 1254 (2022), 132329.

[47] Y. Li, F.-K. Zheng, X.i. Liu, W.-Q. Zou, Guo, C.-Z. Lu, J.-S. Huang, Crystal Structures and Magnetic and Luminescent Properties of a Series of Homodinuclear Lanthanide Complexes with 4-Cyanobenzoic Ligand, Inorg. Chem. 45 (16) (2006) 6308–6316.

[48] S. Sheybani, M. Abbas, H.R. Firouzi, Z. Xiao, H.-C. Zhou, K.J. Balkus, Synthesis of Fluoro-Bridged Ho^{3+} and Gd^{3+} 1,3,5-Tris(4-carboxyphenyl)benzene Metal-Organic Frameworks from Perfluoroalkyl Substances, Inorg. Chem. 62 (10) (2023) 4314–4321.

[49] M. Abbas, A.M. Maceda, Z. Xiao, H.-C. Zhou, K.J. Balkus, Transformation of a copper-based metal–organic polyhedron into a mixed linker MOF for CO_2 capture, Dalt. Trans. 52 (14) (2023) 4415–4422.

[50] T.G. Dastidar, K. Ghosh, M.G.B. Drew, R.M. Gomila, A. Frontera, S. Chattopadhyay, Estimation of the ability of the π-system of pseudohalides (azide and thiocyanate) to participate in CH···π interactions in cyclic hetero-tetranuclear cobalt(III)/sodium and linear trinuclear mixed valence cobalt(III/II/III) complexes, Polyhedron. 222 (2022), 115862.

[51] F.-K. Zheng, A.-Q. Wu, Y. Li, G.-C. Guo, M.-S. Wang, Q. Li, J.-S. Huang, Copper(II), nickel(II) and cobalt(II) complexes of 4-cyanobenzonic acid: syntheses, crystal structures and spectral properties, J. Mol. Struct. 740 (2005) 147–151.

[52] M.B. Coban, A new 3D Ho^{III}-organic framework constructed from 1,3,5-tris(4-carboxyphenyl)benzene and 1,10-phenanthroline: Crystal structure, morphological and solid state luminescence properties, J. Solid State Chem. 317 (2023), 123651.

[53] M. Guan, L. Gao, S. Wang, C. Huang, K. Wang, Syntheses and electroluminescent properties of two europium ternary complexes $Eu(DBM)_3$(PBO) and Eu $(DBM)_3$(PBT), J. Lumin. 127 (2) (2007) 489–493.

[54] J. Jiao, S. Gai, Y. Li, W. Shen, J. Tang, Y. Wang, L. Huang, J. Liu, W. Wang, L. A. Belfiore, $NaYbF_4$:Tb/Eu modified with organic antenna for improving performance of polymer solar cells, Electrochim. Acta. 260 (2018) 959–964.

[55] S. Wang, G. Xie, J. Zhang, S. Zhang, T. Li, Structure, thermal and luminescence properties of Eu/$Tb(BA)_3$phen/PAN fibers fabricated by electrospinning, Opt. Mater. (Amst) 78 (2018) 445–451.

[56] K. Naveen Kumar, J. Choi, Energy-transfer-based NIR photoluminescence of Pr_{3+}/Yb_{3+} co-doped PEO/PVP blended polymer composites, Optik (Stuttg) 208 (2020), 164099.

[57] P. Chen, M. Chai, Z. Mai, M. Liao, X. Xie, Z. Lu, W. Zhang, H. Zhao, X. Dong, X. Fu, F. Ko, X. Shi, W. Zheng, W. Zhou, Electrospinning polyacrylonitrile (PAN) based nanofiberous membranes synergic with plant antibacterial agent and silver nanoparticles (AgNPs) for potential wound dressing, Mater. Today Commun. 31 (2022), 103336.

[58] P. Kumar, S. Singh, I. Gupta, K. Nehra, V. Kumar, D. Singh, Structural and luminescent behaviour of Dy(III) activated $Gd_3Al_5O_{12}$ nanophosphors for white-LEDs applications, Mater. Chem. Phys. 295 (2023), 127035.

[59] P. Kumar, S. Singh, I. Gupta, K. Nehra, V. Kumar, D. Singh, Structural refinement and optical characteristics of single-phase $Gd_3Al_5O_{12}$:Er^{3+} nanophosphors for luminescent applications, J. Lumin. 252 (2022), 119338.

[60] R. Priya, O.P. Pandey, Hydrothermal synthesis of Eu^{3+}-doped Gd_2O_3 nanophosphors and its Judd-Ofelt analysis, Vacuum. 156 (2018) 283–290.

[61] Q.-F. Li, D. Yue, W. Lu, X. Zhang, C. Li, Z. Wang, Hybrid luminescence materials assembled by $[Ln(DPA)_3]_3-$ and mesoporous host through ion-pairing interactions with high quantum efficiencies and long lifetimes, Sci. Rep. 5 (2015) 8385.

[62] C.-H. Gao, L. Zhang, G.-F. Hou, D.-S. Ma, W.-H. Jiang, Y.-H. Yu, Syntheses, structures and properties of chiral Ln(III) coordination polymers based on (R)-4-(4-(1-carboxyethoxy)phenoxy)-3-fluorobenzoic acid, Inorg. Chem. Commun. 78 (2017) 70–73.

[63] Z. Liu, Y. Zhang, B. Chen, X. Zhao, E.Y.B. Pun, H. Lin, Cooperatively Responding Thermal Sensing in Erbium(III)-Functionalized $NaGdF_4$/PAN Crystal-Implanted Fiber, J. Phys. Chem. C. 125 (38) (2021) 21018–21029.

[64] M.A. Sebak, T.F. Qahtan, G.M. Asnag, E.M. Abdallah, The Role of TiO_2 Nanoparticles in the Structural, Thermal and Electrical Properties and Antibacterial Activity of PEO/PVP Blend for Energy Storage and Antimicrobial Application, J. Inorg. Organomet. Polym. Mater. 32 (12) (2022) 4715–4728.

[65] T.P. Mthethwa, M.J. Moloto, A. De Vries, K.P. Matabola, Properties of electrospun CdS and CdSe filled poly(methyl methacrylate) (PMMA) nanofibres, Mater. Res. Bull. 46 (4) (2011) 569–575.

[66] A. Dönmez, Synthesis, Structure and Photoluminescence Analysis of a Ho^{3+}-cluster-based 3D coordination polymer: $\{Ho_2(H_2O)_2(DMF)_2(ATPA)_3\}_n$, J. Clust. Sci. 31 (4) (2020) 887–896.

[67] Y. Yahsi, H. Ozbek, M. Aygun, H. Kara, Crystal structure and photoluminescence properties of a new CdII coordination polymer catena-poly[bis[4-bromo-2-({[2-(pyrrolidin-1-yl)ethyl]imino}methyl)phenolato-κ3N, N′, O]di-μ3-chlorido-di-μ2-

chlorido-bis(methanol-κO)tricadmium(II)], Acta Crystallogr. Sect. C, Struct. Chem. 72 (2016) 426–431.
[68] E. Gungor, H. Kara, Ferromagnetic coupling in two tetranuclear Ni(II) complexes with cubane–like $Ni_4(\mu_3–O)_4$ core: Structure, spectroscopic and luminescence properties, J. Mol. Struct. 1208 (2020), 127859.
[69] E. Gungor, M.B. Coban, H. Kara, Y. Acar, Photoluminescence and Magnetism Study of Blue Light Emitting the Oxygen-Bridged Open-Cubane Cobalt(II) Cluster, J. Clust. Sci. 29 (6) (2018) 967–974.
[70] V. Reddy Prasad, S. Damodaraiah, S.N. Devara, Y.C. Ratnakaram, Photoluminescence studies on holmium(III) and praseodymium(III) doped calcium borophosphate (CBP) phosphors, J. Mol. Struct. 1160 (2018) 383–392.
[71] M.B. Coban, U. Erkarslan, G. Oylumluoglu, M. Aygun, H. Kara, Hydrothermal synthesis, crystal structure and Photoluminescent properties; 3D Holmium(III) coordination polymer, Inorganica Chim. Acta. 447 (2016) 87–91.
[72] A.F. Rogozhin, L.I. Silantyeva, A.N. Yablonskiy, B.A. Andreev, I.D. Grishin, V. A. Ilichev, Near infrared luminescence of Nd, Er and Yb complexes with perfluorinated 2-mercaptobenzothiazolate and phosphine oxide ligands, Opt. Mater. (Amst). 118 (2021), 111241.
[73] J. Chen, Y. Song, Y. Sheng, M. Chang, X. Xie, M.M.A. Abualrejal, H. Guan, Z. Shi, H. Zou, Luminescence properties and Judd-Ofelt analysis of SiO_2:$Ln3^+$ (Eu, Tb) hollow nanofibers fabricated by co-axial electrospinning method, J. Alloys Compd. 716 (2017) 144–155.
[74] J. Hakami, Ü.H. Kaynar, M. Ayvacikli, M.B. Coban, J. Garcia-Guinea, P. D. Townsend, M. Oglakci, N. Can, Structural and temperature-dependent luminescence of Terbium doped $YAl_3(BO_3)_4$ phosphor synthesized by the combustion method, Ceram. Int. 48 (21) (2022) 32256–32265.
[75] M. Jin, N. Li, H. Shao, D. Li, F. Sun, W. Yu, X. Dong, $CaGdAl_3O_7$:Eu^{3+} unidimensional nanostructures: Facile electrospinning synthesis, structure and luminescence, Ceram. Int. 48 (2022) 31548–31558.
[76] C.S. McCamy, Correlated color temperature as an explicit function of chromaticity coordinates, Color Res. Appl. 17 (2) (1992) 142–144.
[77] G.K. Behrh, R. Gautier, C. Latouche, S. Jobic, H. Serier-Brault, Synthesis and Photoluminescence Properties of $Ca_2Ga_2SiO_7$:$Eu3^+$ Red Phosphors with an Intense $5^D0 \rightarrow 7_F4$ Transition, Inorg. Chem. 55 (2016) 9144–9146.
[78] S. Slimi, P. Loiko, K. Bogdanov, A. Volokitina, R.M. Solé, M. Aguiló, F. Díaz, E. Ben Salem, X. Mateos, Structure and luminescent properties of Dy^{3+} activated NaLa9 (SiO4)6O2 yellow-emitting phosphors for application in white LEDs, J. Alloys Compd. 896 (2022), 163109.
[79] W. Li, G. Fang, Y. Wang, Z. You, J. Li, Z. Zhu, C. Tu, Y. Xu, W. Jie, Luminescent properties of Dy^{3+} activated $LaMgAl_{11}O_{19}$ yellow emitting phosphors for application in white-LEDs, Vacuum. 188 (2021), 110215.
[80] A. Mondal, J. Manam, Structural, optical and temperature dependent photoluminescence properties of Cr^{3+}-activated $LaGaO_3$ persistent phosphor for optical thermometry, Ceram. Int. 46 (15) (2020) 23972–23984.
[81] Y.A. Kuznetsova, D.A. Zatsepin, A.F. Zatsepin, N.V. Gavrilov, Temperature-dependent luminescence of intrinsic defects and excitons in nanocrystalline monoclinic Y_2O_3 films, J. Lumin. 250 (2022), 119102.
[82] L. Wu, H. Zhang, W. Zheng, X. Zhang, H.J. Seo, Temperature dependent of luminescence and decay behavior of Eu^{2+} in NASICON-type phosphate $CaZr_4(PO_4)_6$, Mater. Res. Bull. 93 (2017) 245–250.
[83] H.-J. Woo, M. Jayasimhadri, K. Jang, Abnormal temperature dependent luminescence behavior of $CaSrSiO_4$:Eu^{2+} phosphors synthesized via sol-gel strategy, J. Alloys Compd. 703 (2017) 80–85.
[84] W. Huang, D. Wu, D. Guo, X. Zhu, C. He, Q. Meng, C. Duan, Efficient near-infrared emission of a Ytterbium(III) compound with a green light rhodamine donor, Dalt, Trans. (12) (2009) 2081.
[85] F.R. Gonçalves e Silva, O.L. Malta, C. Reinhard, H.-U. Güdel, C. Piguet, J.E. Moser, J.-C.G. Bünzli, Visible and Near-Infrared Luminescence of Lanthanide-Containing Dimetallic Triple-Stranded Helicates: Energy Transfer Mechanisms in the Sm^{III} and Yb^{III} Molecular Edifices, J. Phys. Chem. A. 106 (2002) 1670–1677.
[86] S.A. Bhat, K. Iftikhar, Synthesis and NIR photoluminescence studies of novel Yb(III) complexes of asymmetric perfluoryl β-diketone, J. Lumin. 208 (2019) 334–341.
[87] Y.-X. Chi, Y.-J. Liu, Y. Li, R. Wang, J. Jin, G.-N. Zhang, S.-Y. Niu, Syntheses, structures and near-infrared luminescent properties of a series of Ln(III) coordination polymers, J. Mol. Struct. 1018 (2012) 122–130.